Effect of a ring-shaped laser beam on the weldability of aluminum-to-hilumin for battery tab connectors

Sharhid Jabar; Tianzhu Sun (iD); Pasquale Franciosa (iD); Hiren R. Kotadia (iD); Darek Ceglarek (iD); Bryan Paolini; Richard Faulhaber

Check for updates

CrossMark

View Online

Export Citation

Effect of a ring-shaped laser beam on the weldability of aluminum-to-hilumin for battery tab connectors

Sharhid Jabar,[1] Tianzhu Sun,[1] (iD) Pasquale Franciosa,[1] (iD) Hiren R. Kotadia,[1,2] (iD) Darek Ceglarek,[1] (iD) Bryan Paolini,[3] and Richard Faulhaber[3]

AFFILIATIONS

[1]Warwick Manufacturing Group, The University of Warwick, Coventry CV4 7AL, United Kingdom
[2]School of Engineering, Liverpool John Moores University, Liverpool L3 3AF, United Kingdom
[3]Lumentum Operations LLC, Commercial Lasers, San Jose, California 95131

ABSTRACT

Advances in laser beam shaping technologies are being studied and are considered beneficial in many aspects of dissimilar metal joining, which include reducing intermetallic compounds (IMCs), optimizing weld pool profiles, and controlling porosity and spatters. This paper utilizes a coaxial ring and core dual beam laser and aims to study the impact of the power ratios between core and ring beams on the weldability of 1100 aluminum alloy to hilumin (steel). High-resolution electron microscopy was performed in the cross sections of the weld pools to quantify the melt pool composition and subsequent IMC formation and weld defects (cracking and cavitation). Lap-shear mechanical testing and electrical resistivity testing were also carried out. Results showed that the optimal power ratio for lap-shear strength was 0.4 (intermediate core and ring) due to the reduction in the Fe-rich liquid into the upper weld region. As a result, this produced a smaller interface between the Fe-rich region and Al, thus reducing the formation of the most detrimental IMC (e.g., Fe_2Al_5). Conversely, a power ratio of 0.2 (core-dominant) was found beneficial for reducing electrical resistance due to a reduced total IMC volume.

Key words: laser welding, battery tab manufacturing, dissimilar metal welding, laser beam shaping, ring and core dual beam, intermetallics.

I. INTRODUCTION

In electric vehicles (EVs), the structure of a battery pack follows a cell-module-pack layout to achieve the desired energy density and packaging requirements, and the connection between cells plays a critical role.[1] For the individual cells, the casings are typically made of electrolytically nickel-plated cold-rolled strip steel (commercial name: hilumin[2]) due to good formability and sufficient mechanical properties, and the hilumin is typically of ≤0.5 mm in thickness. Individual cells are interconnected via a thin sheet (≤0.5 mm), which is commonly known as a "busbar tab" or "tab."[3] The joining of cells to busbar tabs is done through fusion welding techniques, such as laser beam welding (LBW),[4] microspot welding,[5] and ultrasonic welding,[6] and is often referred to as "tab welding." LBW is often the preferred option due to several notable advantages, such as being a noncontact process, high speed with the ease of automation, low heat input, and improved quality control after optimization.[7]

The material selection of the tab is based on several properties, with the most important being electrical and thermal conductivity while the remaining being cost-effective at the low weight. Table I summarizes the key performance criteria and properties for possible busbar tab materials. Ni has good mechanical properties and has good weldability with steel; however, it is also quite expensive and has a higher electrical resistance than Cu and Al. Cu possesses excellent electrical properties, and it forms a good metallurgical

TABLE I. Key performance criteria and properties of the common materials used for busbar tabs in EV battery welding.

Property	Ni	Fe	Cu	Al
Weldability with steel/iron (Ref. 9)	Good	Excellent	Good	Low
Cost (relative to steel)	High	—	High	Fair
Density (g/cm^3)	8.90	7.90	8.92	2.80
Electrical resistivity at 20 °C ($\mu\Omega$ m)	0.067	0.097	0.017	0.026
Thermal conductivity (W/m k)	97.5	57.8	391.1	231.0
Thermal expansion at 20 °C (μK^{-1})	13.4	12.1	16.9	24.0
UTS (MPa)	345	320–400	200–360	100–150

bond with steel; it also forms very little intermetallic compounds (IMCs). This is due to the formation of an immiscible alloy system during solidification, which means that the two metals do not mix homogeneously but instead form separate phases due to the limited solubility between the two. However, Cu-to-steel joints are prone to corrosion without the application of a coating; furthermore, Cu can be quite costly. In contrast, 1xxx series aluminum,[4,8] consisting primarily of pure aluminum, is a viable alternative to Cu to reduce weight and material costs while maintaining good electrical conductivity. However, the fusion joining of aluminum and steel (Fe) has one major setback, which is the formation of brittle IMCs of the Fe$_x$Al$_x$ type.[7]

Many pairs of dissimilar metals used in fusion joining applications form IMCs and other solid solutions of limited solubility. There are three conditions that need to be met in order to have complete solid solubility between two different metals:[10] (1) the crystal lattice structure must be of the same type; (2) the atomic diameters must not differ by any more than 8%–15%; and (3) the electrochemical properties must be similar, which is observed via their electronic structure of the atoms. Al and Fe (the main constituent of steel) do not satisfy these criteria and for that reason, the main issue that affects the welding of Al to steel (or steel to Al) is the formation of brittle IMCs, which can cause a significant loss in mechanical and electrical properties of the weld.[11] Information on the crystal structures and microhardness mechanical properties of common Fe$_x$Al$_x$ IMCs in the Fe–Al system is shown in Table II. The extremely high micro-hardness of these IMCs makes them very brittle and is often the cause of the nucleation and propagation of cracks at the steel and Al weld interface. Furthermore, the differences in crystal structures and thermal expansion coefficients can lead to considerable mechanical and thermal stresses during the solidification process of the weld, resulting in the formation of defects (cracks and cavities).[12] With regard to the electrical properties of IMCs, a few studies on Cu to Al laser welds[13,14] have shown that the formation of IMCs (Al$_x$Cu$_x$-type) has a negative influence on the weld's ability to conduct electricity. This is due to the type of atomic bonding; in the base metals, the metallic bonds allowed the flow of electrons relatively easily with little resistance, whereas the IMCs have covalent bonds, which means the valence electrons require a lot more voltage or temperature. Table II shows the type of crystal structures for Fe$_x$Al$_x$ IMCs, the more complex crystal structures conduct electricity less efficiently as compared to the more ordered crystal structures.

Seffer et al.[16] investigated the configurations of overlap welding with both Al and steel on top, and the results showed that

in the steel on top configuration, weld efficiency improved (less laser power is required compared to Al on top) and the Al-rich IMC content reduced. Conversely, with the Al on top configuration, higher temperatures must be reached directly in the Al side in order to penetrate through the steel sheet; this leads to excessive heating and melting of Al as well as uncontrolled mixing at the interface. If the IMCs are uniformly distributed throughout the metal (between the grains), a benefit in strength and grain refinement can be found, as demonstrated in Ref. 17, where Al solute migrated into the upper steel sheet while welding with the adjustable ring-mode (ARM) laser. The type and amount of IMC can have a significant influence on mechanical properties. When the IMC layer is continuous along the weld interface and is over 10 μm in thickness, it is widely considered detrimental.[18] This, however, is only really possible in a shallow conduction mode welding mechanism in which the steel or Al do not significantly penetrate each other, as shown in previous research works[10,17]—to satisfy a high penetration keyhole mode welding mechanism, the mixing of steel and Al significantly increases, leading to a range of IMCs spread across the entire weld pool.

Laser beam shaping is gaining popularity since it allows controlled cooling rates and thermal gradients in and around the molten pool via spatial and temporal modulation of the heat input. Benefits have been reported in improved seam quality,[19] reduced spatters/porosity, and improved keyhole stability.[20] However, only few attempts with scattered results have studied the impact of laser beam shaping on intermetallic phase formation. For steel to Al welding, beam shaping has shown a positive effect to reduce the IMC layer thickness[17] and improved homogeneity of the IMC layer.[21] This paper utilizes coaxial ring and core dual beam laser and aims to study the impact of the power ratios between core and ring beams on weldability of 1100 aluminum alloy to hilumin. The

TABLE II. Properties of the common IMCs found in the Fe–Al system (Ref. 15).

IMC type	Crystal structure	Micro-hardness (HV)
Fe$_3$Al	Ordered BCC	250–350
FeAl	Ordered BCC	400–520
Fe$_2$Al$_7$	Complex BCC	650–680
FeAl$_2$	Complex rhombohedral	1000–1050
Fe$_2$Al$_5$	BCC orthorhombic	1000–1100
FeAl$_3$	Highly complex monoclinic BCC	820–980
Fe$_4$Al$_{13}$	Complex BCC	—

relevance of this study relates to the fact that only very limited experimental data are available on the weldability of 1100 aluminum (0.5 mm) to hilumin (0.5 mm) with beam shaping (ring and core) technology. Material-mixing and IMC formation are studied to explore the effect of the ring-shaped laser beam on the material response, with subsequent analysis on cracking behavior, mechanical (lap-shear) properties, and electrical resistivity.

II. MATERIALS AND METHODS

A. Materials and welding procedure

LBW was performed on 1100 aluminium alloy to hilumin (both 0.5 mm), in an overlap configuration, with coupons of 70 mm by 20 mm in length and width, respectively. Chemical compositions of the two materials are provided in Table III.

Welding experiments were conducted using a 4 kW Lumentum CORELIGHT laser,[23] which had a 50 μm core diameter and a 200 μm ring diameter and a BPP of 1.4 and 11 mm mrad for core and ring, respectively. The laser fiber was coupled to the Scansonic RLW-S (Fig. 1) welding head (Scansonic MI GmbH, Germany), which comes with a 200 mm collimating length and a focal length of 400 mm. The resulting Rayleigh length is 1.8 and 5.2 mm for the core and ring, respectively.

The power ratio between the two laser beams was defined by a beam splitting system (BSS), with BSS=0 corresponding to a core-only beam, and BSS=1 to a ring-only beam. Beam caustic profiles and power distributions were experimentally measured via a PRIMES focus/power meter, with results shown in Fig. 2. The welding speed was fixed at 240 mm/s. The effect of power ratio and total power were investigated in this study: power was varied from 1200 to 2800 W at 200 W increments; power ratios were used from 0 to 1 in 0.2 increments. The laser beam was focused on the top surface of the workpiece and no beam oscillation/wobbling, shielding gas or filler wire was used.

B. Microstructural characterization

A standard metallographic procedure was carried out to produce three cross sections from each weld seam. This involved steps of sectioning, mounting in conductive resin, grinding until flat and then polishing in sequential steps of 9, 3, and 0.02 μm diamond solutions and polishing cloths. The microstructure of the welds was characterized after welding using optical and scanning electron microscopy (SEM). Optical images for each cross-section were taken using a Keyence VHX7000 light microscope. This allowed the quantification of the weld geometries and crack
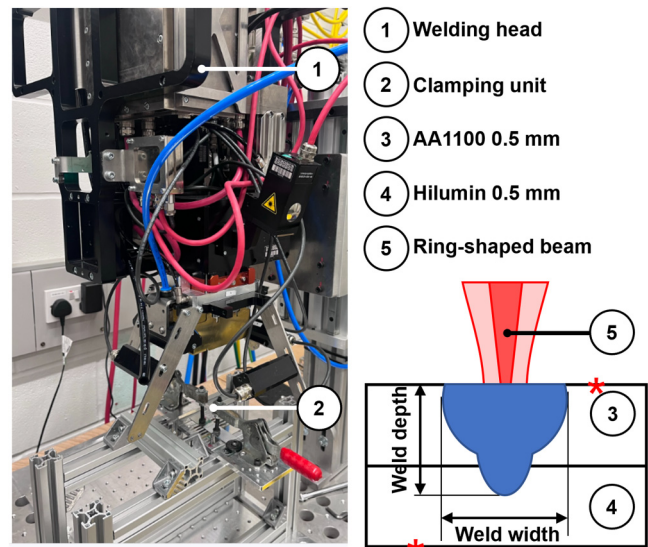

FIG. 1. Laser welding setup with the schematic of a weld cross section.

thicknesses; for the former, measurements were taken from the three cross sections, and for the latter, 10 equally spaced measurements were taken from each of the three cross sections. Crack thicknesses were characterized into five categories: (1) *minimal cracking* (<10 μm), (2) [10, 20[μm, (3) [20, 30[μm, (4) [30, 40 [μm, and (5) *excessive cracking* (>40 μm). SEM was used for backscattered electron (-BSE) imaging and chemical mapping using an energy dispersive x-ray spectroscopy (-EDS) detector. An accelerating voltage of 20 kV along with a current of 11 nA and dwell time of 250 ms allowed for a sufficiently high-count rate and high-resolution chemical maps. Line scans were performed based off the SEM-EDS data, these were 50 μm in thickness and were from top to bottom of the weld seam cross section.

C. Mechanical and electrical testing

Lap-shear mechanical testing (ASTM) was performed on the welded coupons using a 30 kN Instron tensile testing machine—for each weld ID three replicas were carried out. Electrical resistivity measurements were acquired using a resistivity measurement device, for each weld ID, three measurements were recorded. The resistance (in mΩ) was measured diagonally across each weld seam, with a distance of 2 mm from the weld seam (top and bottom)—the red asterisks in Fig. 1 mark these approximate locations.

III. RESULTS AND DISCUSSION

A. Metallographic analysis

For the core-dominant power ratios (BSS = 0–0.4), a lower total power was enabled—this was because the core-dominant beam provided a much greater power density due to the smaller beam waist. This, in turn, gave a more penetrative effect vertically, rather than laterally compared to the ring-dominant beam. Similar results have

TABLE III. Chemical compositions of the Ni-coated hilumin steel and 1100 aluminum alloy (Ref. 22).

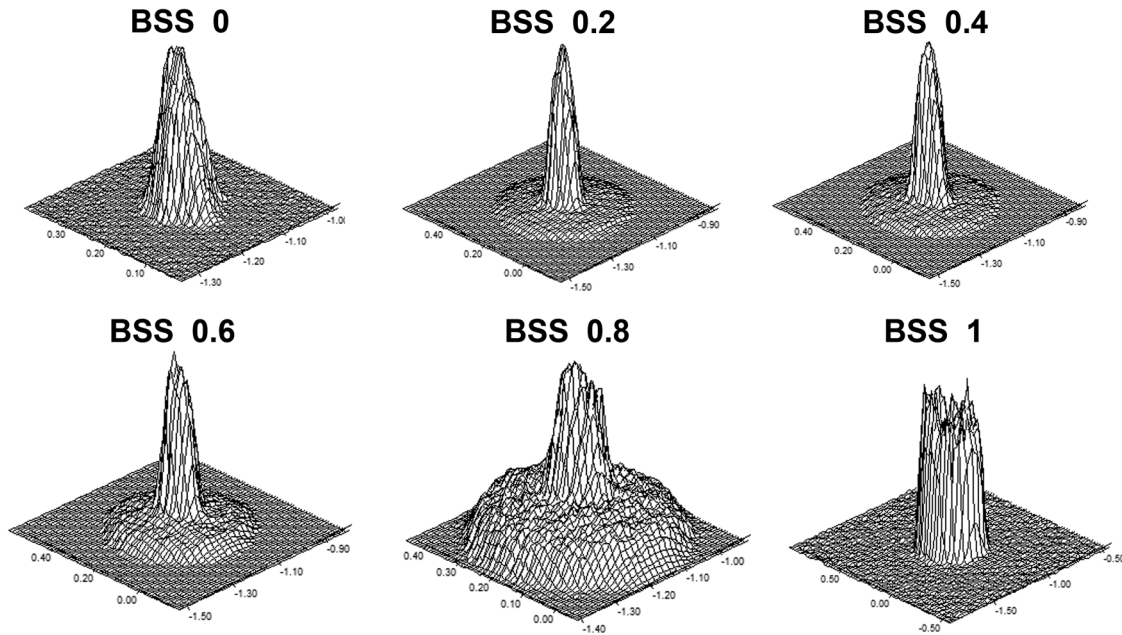| Composition (wt. %)						
	Fe	C	Mn	Al	Si	S
Hilumin	Bal.	0.047	0.24	0.06	0.002	0.01
	Al	Si	Fe	Cu	Mg	Zn
AA1100	Bal.	0.95	0.9	0.01	0.05	0.1

FIG. 2. Power distributions (not to scale) of the Lumentum CORELIGHT laser for the tested BSS.

been found in other research.[17] The color scheme in Table IV was used to categorize each of the weld IDs based on their average crack thicknesses observed in the three cross sections. Since most of the cracks in these welds were continuous, the measurement of the thickness allowed a clear distinction. The welds with "minimal" cracking mostly contained thin hair-line cracks, whereas those with excessive cracking contained thick cracks, representing a cavitation-like structure. The extent of cracking was deemed the main factor for the initial assessment of the weld quality.

At power levels below 2600 W and BSS = 1, no connection was found between the sheets; furthermore, excessive cracking was observed for BSS > 0.8 and laser power above 2400 W. Conversely, at BSS = 0 excessive cracking was common at many different power levels (1200–2400 W); this signified that the use of just the core-dominant beam or just the ring-dominant beam was not sufficient in producing high-quality welds. The optimal power ratio was found in the range BSS = 0.2–0.6 at power 2400–2600 W. Figure 3 shows the cross sections for the identified optimal process window. It is observed that at both power levels, the penetration of the weld increases with decreasing power ratio (toward core-dominant). At the highest power ratio (ring-dominant) and 2400 W, the power density is not enough to form a successful bond between the two

TABLE IV. Welding matrix showing the tested welding parameters in bold black cells. Dashed cell borders show the weld IDs that were analyzed in detail.

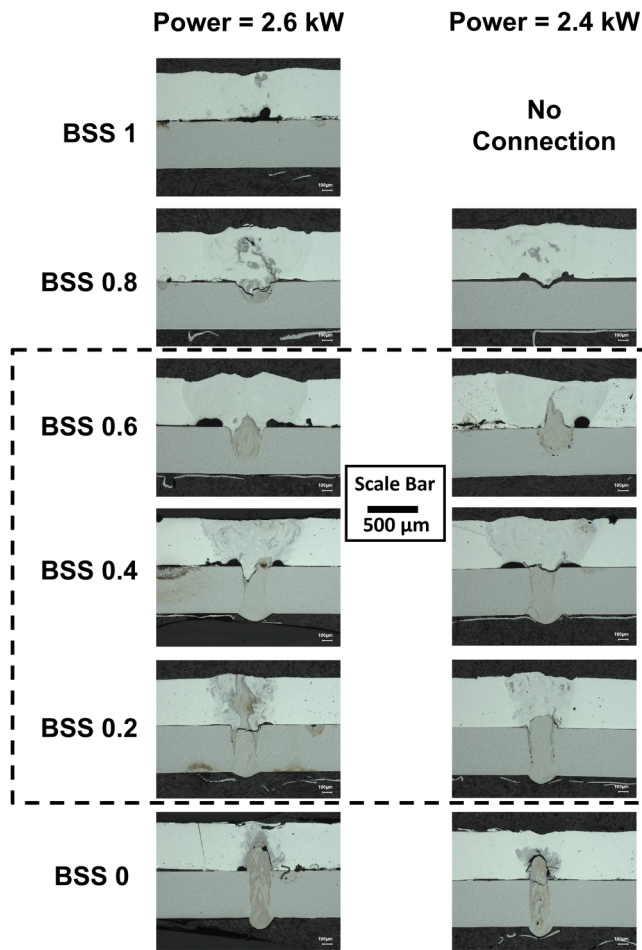| Total Power (W)	BSS power ratio						Colour code for cracking classification		
	1	0.8	0.6	0.4	0.2	0			
2800							Minimal (< 10 μm)		
2600			ID1	ID 2	ID 3		Between 10 and 20 μm		
2400			ID 4	ID 5	ID 6		Between 20 and 30 μm		
2200							Between 30 and 40 μm		
2000							Excessive (> 40 μm)		
1800									
1600									
1400									
1200									

FIG. 3. Optical micrographs showing representative cross sections for the weld IDs with varying BSS = 0–1 and total powers of 2400 and 2600 W. The dashed box shows the welds that were further analyzed in detail.

sheets. As already found in Ref. 17, the combined power density of core and ring beams plays a critical role in controlling the fusion zone and the material-mixing, hence the formation of IMCs. Sections III B–III F will focus on the trials highlighted in the dashed cells in Table IV—samples with lower crack thickness compared to others.

B. Material-mixing and IMC formation

For each of the power ratios, the interaction of the laser beam with the materials was distinctive in terms of the mixing of Al and Fe and subsequent IMC formation. Although the steels possessed a Ni-coating, Ni was omitted from this study because of the relatively low amount of it (approximately $10\,\mu m$ in thickness) compared to the base materials and was not considered to significantly affect the weld pool characteristics. For the key welding trials highlighted in Fig. 3 (BSS = 0.2–0.6 and total powers of 2400 and 2600 W),

SEM-EDS chemical mapping was performed to understand the mixing of the two metals. Line scans were performed along the center of the cross sections for quantitative analysis (Fig. 4). For these maps, the main alloying elements of steel (Fe) and the 1100 aluminum alloy (Al) were analyzed. The SEM-EDS maps displayed the weld pool morphologies and material-mixing due to the different power ratios.

For the higher power ratios of 0.6, a wider weld pool was generated with less penetrative effects; however, the migration of Fe into the upper sheet was limited due to less recoil pressure and fluid-flow generated by the low power density.[17] The line-scan data [Fig. 4(g)] show the change in composition for the welds at BSS = 0.6: from the top of the weld, there is evidently very little mixing of Fe and Al. For both trials (at 2600 and 2400 W), the compositions start with 90 wt. % Al and 10 wt. % Fe. At this composition, the eutectic phase $FeAl_3$ is identified through SEM-BSE imaging and EDS chemical mapping [Fig. 5(a)i and 5(a)ii]. Although some Fe_4Al_{13} phase was found very sparsely around the top of the weld pool [Fig. 5(a)], a sharp transition is found when the Fe rich region begins, which leads to approximately 20 wt. % Al and 80 wt.% Fe.

At BSS = 0.4, the power density is greater due to a more core-dominant laser when compared to BSS = 0.6. This, in turn, led to more Fe migrating into the top sheet of the weld, which can be observed by the darker hue in the EDS maps [Fig. 4(b) and 4(e)]. Further to this, the line scans performed for BSS = 0.4 [Fig. 4(h)] show a greater content of Fe (15–20 wt. %) at the top of the weld. It should, however, be noted that the Fe-rich region is prevented from travelling into the top of the weld, unlike with the welds at BSS = 0.6 and 0.2.

At the lowest of the three power ratios, BSS = 0.2, the recoil pressure is the greatest due to the core-dominant beam. Furthermore, the greater power density leads to a higher amount of melting of steel as compared to the ring-dominant welds. At higher temperatures, the steel becomes less dense and creates buoyancy forces, which encourage the flow of liquid. The lower surface tension of the molten Al, when compared to the molten steel also induces Marangoni forces. These mechanisms collectively allow more migration of steel into the upper sheet. Large amounts of Fe can be observed in the top area of the weld pool. Subsequently, the increased concentration of Fe in the top of the welds for BSS = 0.2 and 0.4 lead to the formation of more IMCs in the form of Fe_4Al_{13}, which can be characterized by a high Al concentration and needle-like morphology in Fig. 5(c)i. When comparing the distribution of the Fe_4Al_{13} phase from the 0.4 and 0.2 power ratios, it is found that for BSS = 0.4, Fe_4Al_{13} is more densely packed [Fig. 5(b)], in comparison to BSS = 0.2, the Fe_4Al_{13} is found more sparsely scattered around the top of the weld pool [Fig. 5(c)].

C. Mechanical and electrical properties

The mechanical strength (measured as lap-shear strength) and electrical resistance are two key properties for characterizing the performance of the welds. For the key welding trials highlighted in Fig. 3 these properties were measured and displayed in Fig. 6. No significant relationship was found between the lap-shear strength and electrical resistivity. However, electrical resistivity increased
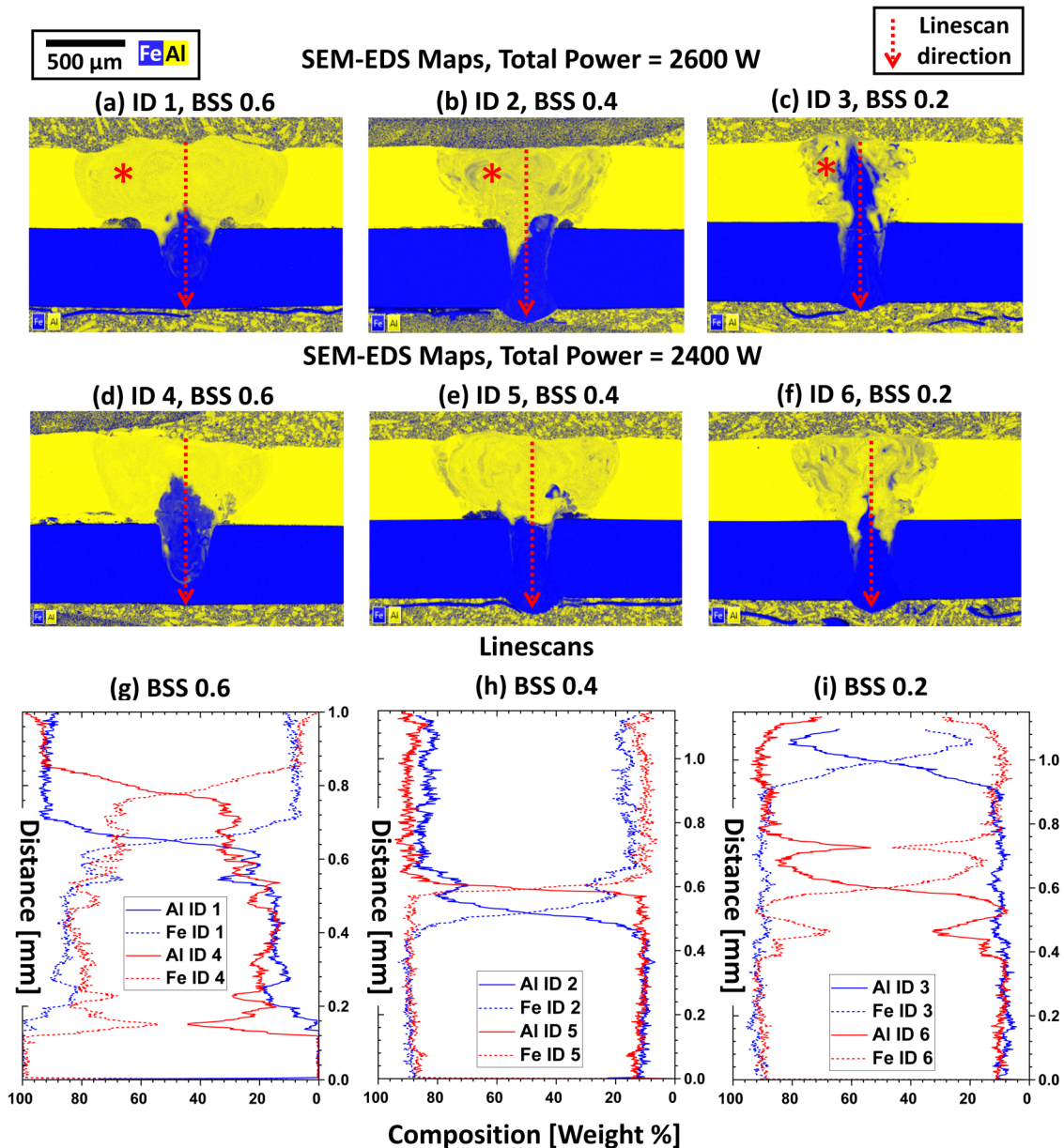
FIG. 4. SEM-EDS chemical mapping data (a)–(f) and corresponding line-scan data (g)–(i). The asterisk marks the location of the smaller SEM-EDS maps in Fig. 5.

with increasing power ratio (from 0.2 to 0.6); furthermore, the mechanical strength was found to be the greatest at BSS = 0.4 [Fig. 6(a)]. At power levels of 2600 and 2400 W, the lap-shear strengths were measured at 30.6 and 31.8 N/mm, respectively, and for both welds, the width was over 1 mm [Fig. 6(a)]. A power ratio of 0.4 was considered optimal when compared to 0.2 and 0.6 due to two main reasons: (1) the presence of a relatively wide weld pool at the interface; (2) Fe-rich region was prevented from penetrating

up into the top of the weld when compared to the other two power ratios (0.6 and 0.2). This can be seen quite clearly in the SEM-EDS chemical mapping in Fig. 4. The smaller interface of the Fe-rich material and Al meant less Fe_2Al_5 formed, which commonly grows at the interface between these two materials and is considered responsible for the nucleation of cracks.[24]

The electrical resistivity can be related to the morphology of the welds—Fig. 6(b) compares the weld width to the electrical
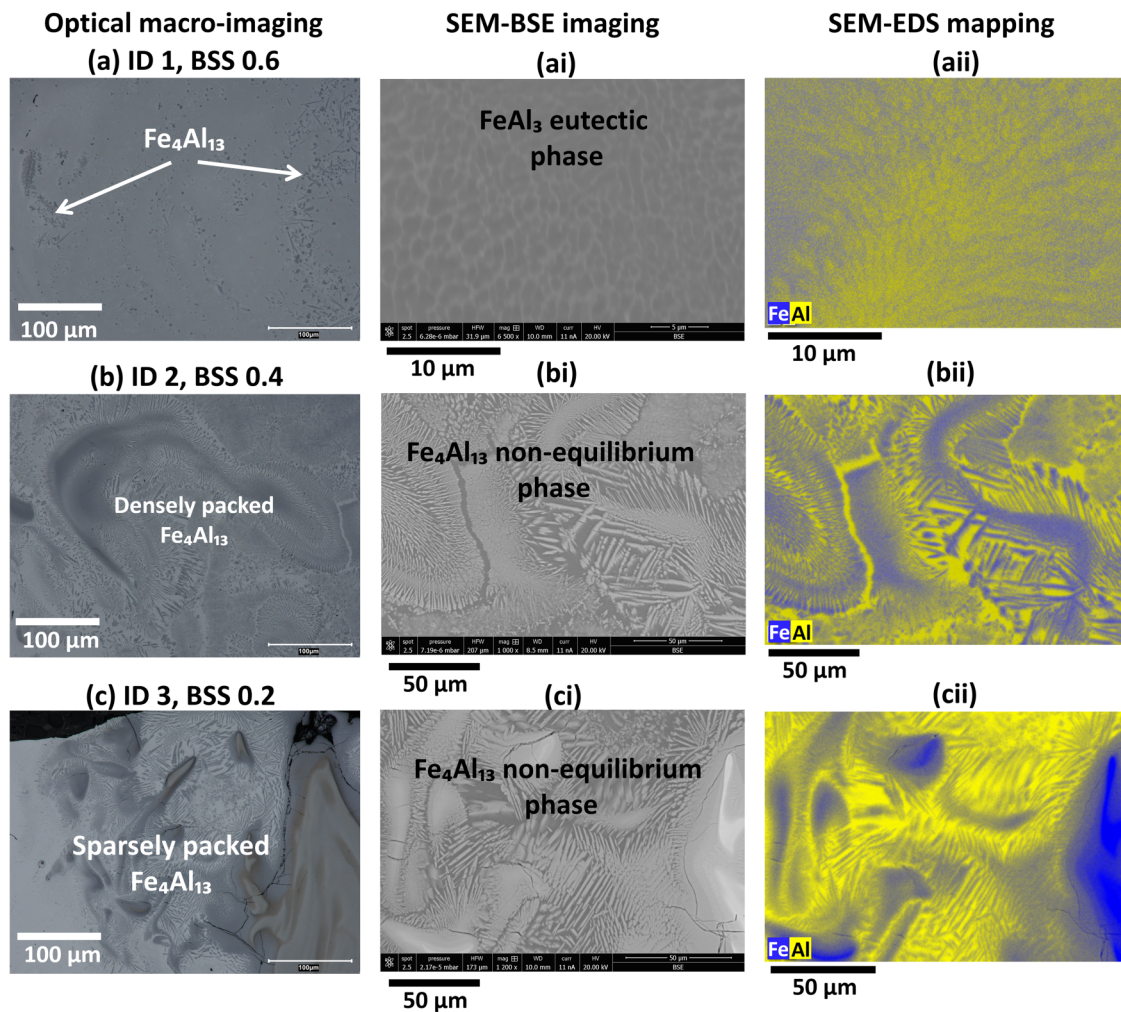
FIG. 5. Optical microscope images showing the weld microstructure (a)–(c), SEM-BSE images showing the microstructure of the welds in the Al sheet [(a)i–(c)i] and corresponding SEM-EDS chemical maps [(a)ii–(c)ii]. Locations taken from the asterisk are marked in Fig. 4.

resistivity. For the welds with the greatest electrical resistivity (BSS = 0.6), the weld width was also the greatest, approximately 1.2 mm, whereas for the welds with the lowest electrical resistivity (power ratio 0.2), the weld widths were also the lowest (0.6–0.8 mm). However, it should be noted that the spread in the data was very high, this shows a stable weld was difficult to achieve in comparison to the higher power ratio welds (0.4 and 0.6). This can be due to the less efficient keyhole stabilization from the core-dominant beam at a power ratio of 0.2.[20]

D. Cracking in the weld pool

Fractography analysis showed the cracks in the welds commonly initiated via the interface of the Fe_2Al_5 phase and the surrounding weld matrix, which then propagates along the length of the IMC and into other IMCs. Fe_2Al_5 is typically found at the interface of steel (Fe-rich material) and Al and at a composition of approximately 55 wt. % Al from the Fe–Al binary phase diagram.[25] In Fig. 7(b), the cracks can be seen to form into the Fe-rich matrix, via Fe-rich IMCs, typically $FeAl_2$ of approximately 60 wt. % Fe; large cavities can be observed, which can be due to the differences in thermal expansion coefficients during the solidification of the different components of the weld, i.e., Al, steel, and IMCs. Figure 7(a) shows an example of cracking in the "minimal state" or when referring to Table IV, an example can be ID 1. While Fig. 7(b) shows an example of an "excessively" cracked weld, which can be seen as power ratio 0 and total power of 2200 W from Table IV.

The formation of Al-rich IMCs (i.e., $FeAl_3$, Fe_4Al_{13}, and Fe_2Al_5) is highly undesirable due to them being more brittle than Fe-rich IMCs (i.e., Fe_3Al, FeAl). However due to the Al on top
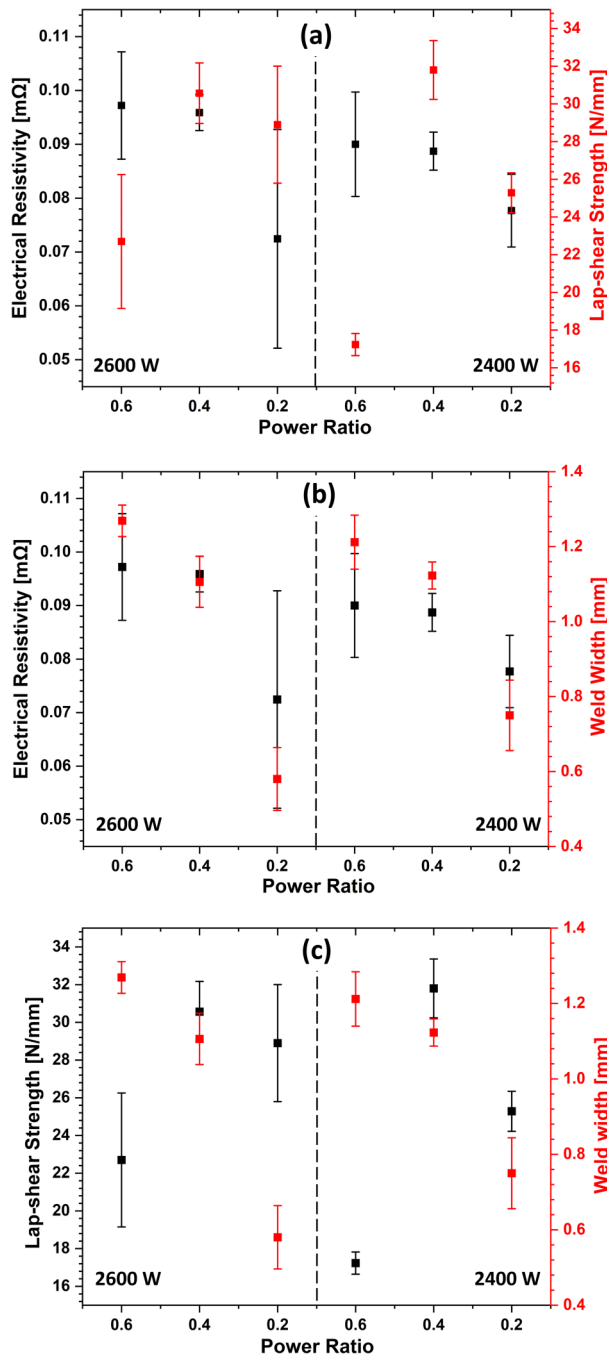
29 November 2023 14:30:58

FIG. 6. Graphs comparing the electrical resistivity of the welds vs the lap-shear strength (a), weld width (b), and lap-shear strength vs weld width (c).

configuration used in this study, the formation of Al-rich IMCs are more abundant when compared to similar processes with steel on top.[16,17] Further to this, Al-rich IMCs are more likely to form during welding, and this is due to the lower enthalpy of the

reaction. The Fe_2Al_5 IMC was found for crack initiation and propagation in all cases of welding, the formation and growth of Fe_2Al_5 is quite rapid due to a high amount of vacancies along its crystallographic axes (perpendicular to the plane of the IMC).[26] For this reason, a thick and planar layer is often found at the interface of Fe–Al laser welds in all welding configurations, and the Fe_2Al_5 IMC is typically found for the initiation of cracks in Fe–Al fusion joints.[24]

E. Discussion on the IMC formation

The mixing of Fe and Al was distinctly different at the three analyzed power ratios (BSS = 0.2, 0.4, and 0.6). During keyhole mode welding, the part of the material is vaporized, for this phenomenon to occur the power density must be sufficient to penetrate the materials. Due to this large increase in recoil pressure a thin cavity forms, which is referred to as the "keyhole."[26] The important factor in this process is the power density provided by the laser beam.

In the current study, the use of the ring and core beam significantly changes the delivery of the power, with the ring providing a more lateral power input as displayed in Fig. 2. From Fig. 4, it was clear that the lower power ratios produced more recoil pressure and buoyancy forces on the molten material due to a greater power density generated from the core-dominant laser beam. In addition to this, the difference in surface tensions also induces fluid-flow via Marangoni forces. This leads to the migration of Fe into the top of the weld pool. For the cases with a power ratio of 0.6, the eutectic IMC phase $FeAl_3$ was produced. This can be found on the Fe–Al binary phase diagram,[25] which is shown in Fig. 8, marked by the red asterisk (1.85 wt. % Fe at 655 °C). The eutectic reaction can be defined by the formation of two solids from one liquid phase as detailed in Eq. (1),

$$Al\ (l) + Fe\ (l) \rightarrow FeAl_3(s) + Al\ (s). \qquad (1)$$
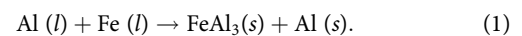
From Fig. 5(a), the grain boundary eutectic IMC phase $FeAl_3$ can be seen as a lighter shade on the grain boundaries. Due to atomic number (Z) contrast between the $FeAl_3$ and the Al matrix. For the power ratios of 0.4 and 0.6 as mentioned previously, more fluid-flow allows the migration of Fe into the top of the weld. When studying the Fe–Al phase diagram (Fig. 8), the solidification of the alloy moves further to the left from the eutectic point due to a greater Fe content. Highlighted as the metastable IMC phase Fe_4Al_{13}, although less thermodynamically stable than the other IMC phases in the Fe–Al system, it can form under high temperatures, which is highly likely due to the high-temperatures during laser welding. The Fe_4Al_{13} IMC phase can also be characterized by its needlelike morphology and ~80 wt. % Al content.

F. Discussion on the electrical performance

The electrical resistance was found to increase with increasing power ratios, from 0.2 to 0.6. A significant increase in resistance was found when the power ratio increased from 0.2 to 0.4. When comparing the weld widths to the resistance measurements, this can be explained by the large increase in the weld width, which is

SEM-BSE imaging

SEM-EDS mapping
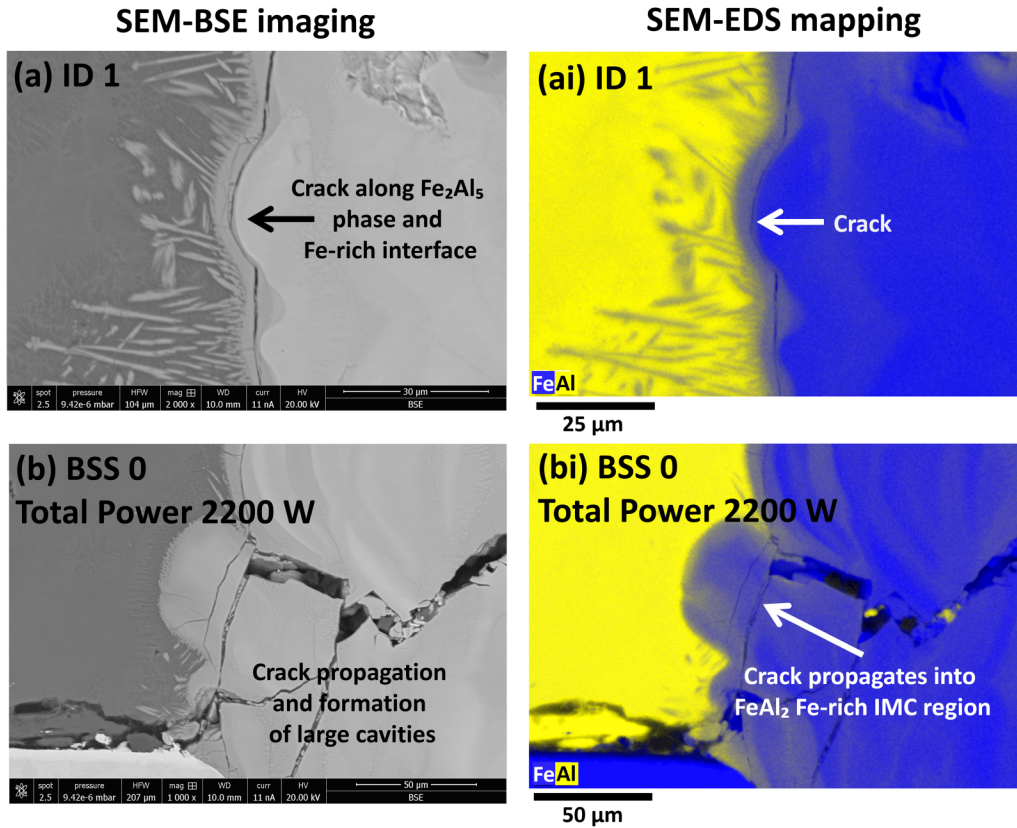

FIG. 7. SEM-BSE images showing examples of cracks in the welds [(a) and (b)] and corresponding SEM-EDS chemical maps [(a)i and (b)i].
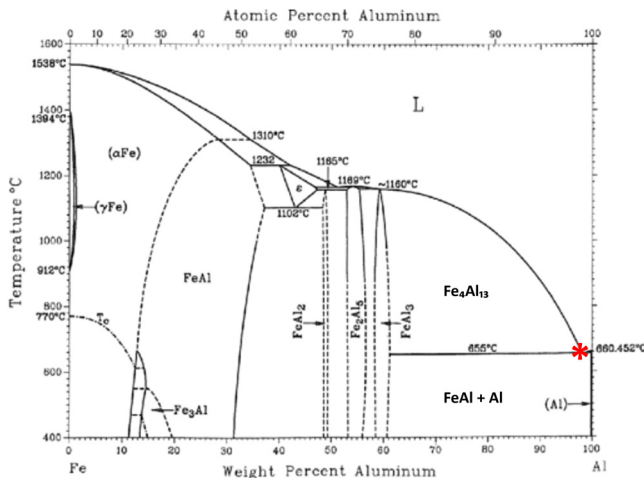

FIG. 8. The Fe–Al binary phase diagram (Ref. 25) to support the discussion of the IMC formation.

also found when increasing the power ratio from 0.2 to 0.4, for both 2400 and 2600 W welds. Findings are discussed as follows:

(1) The mixing of Fe and Al and subsequent formation of Fe_xAl_x IMC compounds, for which clearly the increase in weld width means the formation of a larger inhomogeneous region, albeit at less magnitude. Wang et al.[13] found that the increased formation of IMCs in Cu to Al laser welded joints led to a greater electrical resistivity, this was believed to be due to the stronger covalent bonds in IMCs versus the metallic bonding in the base metals. The covalent bonds required a lot more energy for the valence electrons to move in order to form a current. Similarly, Schmalen and Plapper,[14] found the electrical resistance in Al to Cu overlap welds increased when a greater amount of IMC was formed in the weld pool. The authors described the reasoning due to the increased amount of material-mixing due to the use of laser beam oscillation during welding. In the current study, the amount of total IMC volume is clearly greater in the higher power ratios [Fig. 5(a)–5(c)]; at the power ratio of 0.2, the IMC in the top of the weld pool can be quite clearly sparsely distributed and in the lower total

29 November 2023 14:30:58

amount as compared to the larger weld pools of the power ratios 0.4 and 0.6.

(2) The changes in the microstructure of the base metal may also influence the electrical resistance through grain refinement. The rapid cooling associated with laser welding means the grain growth is restricted during cooling, this can also be seen in Fig. 5(a) for which the grain size of the Al is approximately 2.5μm. The finer grains mean more grain boundary length and can hinder the electron travel through the material due to differences in atomic arrangements at grain boundaries compared to grain interiors, therefore, increasing the resistance.[27]

IV. CONCLUSIONS

This study has investigated the influence of ring-shaped laser beams on the weldability of 1100 aluminum alloy to hilumin steel. Findings have been presented by considering three key power ratios between the core and ring beam. It was found that the suitable selection of the core/ring power ratio is a key parameter to control metallurgical bonding and mechanical and electrical properties. Two main conclusions have been drawn.

(1) Examination of the material-mixing and IMC formation showed that at lower power ratios (0.2 and 0.4), the increased power density of the laser resulted in a large amount of Fe migration to the top of the weld pool due to greater recoil pressure and fluid-flow. This meant the metastable IMC phase Fe_4Al_{13} was prominently found in the top portion of the weld. In comparison, at the power ratio of 0.6, the ring-dominant beam reduced the turbulence of the fluid-flow, resulting in less Fe mixing into the top of the weld, promoting the formation of the eutectic IMC phase $FeAl_3$ on the aluminum matrix grain boundaries. However, it should be noted that the total IMC volume in both 0.4 and 0.6 power ratio welds was greater than the power ratio of 0.2 due to the formation of a considerably wider weld pool.

(2) Lap-shear testing was performed and the power ratio of 0.4 showed the highest strengths of 30.6 and 31.8 N/mm at total powers of 2600 and 2400 W, respectively. However, the power ratio of 0.4 was considered optimal because of two reasons: (a) the formation of a wide weld pool (approximately 1.1 mm) and (b) while preventing the migration of the Fe-rich material progressing into the top of the weld, the latter was responsible for reduced formation of the most detrimental IMC, Fe_2Al_5. For the electrical resistivity measurements, the narrower weld pool formed from the core-dominant power ratio 0.2 showed the least resistance. This was due to a smaller welded region, which meant less total IMC volume.

Future work will complement experimental studies with advanced multiphysical CFD simulations to better understand the mechanisms behind the material-mixing and diffusion processes and provide information about temperature/pressure fields and fluid-flow and help elucidate the impact of beam shaping on phase formation during dissimilar metal joining.

AUTHOR DECLARATIONS

Conflict of Interest

The authors have no conflicts to disclose.

Author Contributions

Sharhid Jabar: Conceptualization (equal); Data curation (lead); Formal analysis (lead); Investigation (equal); Methodology (equal); Software (equal); Validation (equal); Visualization (equal); Writing – original draft (lead); Writing – review & editing (equal). **Tianzhu Sun:** Conceptualization (equal); Investigation (equal); Methodology (equal); Supervision (equal); Visualization (equal); Writing – review & editing (equal). **Pasquale Franciosa:** Conceptualization (equal); Data curation (equal); Formal analysis (equal); Funding acquisition (lead); Investigation (equal); Methodology (equal); Project administration (equal); Resources (equal); Software (equal); Supervision (lead); Writing – review & editing (lead). **Hiren R. Kotadia:** Visualization (supporting); Writing – review & editing (supporting). **Darek Ceglarek:** Funding acquisition (equal); Project administration (equal). **Bryan Paolini:** Project administration (supporting); Resources (lead). **Richard Faulhaber:** Resources (equal).

REFERENCES

[1] Wayne Cai, "Lithium-ion battery manufacturing for electric vehicles: A contemporary overview," in *Advances in Battery Manufacturing, Service, and Management Systems* (Wiley Online Books, New York, 2018), pp. 209–213.

[2] Tata Steel, see http://www.tatasteeleurope.com/static_files/Downloads/General/Industry/Strip/Electro Plated/1462 TATA Hilumin.pdf for "Hilumin®" (2013).

[3] G. Chianese, S. Jabar, P. Franciosa, D. Ceglarek, and S. Patalano, "A multiphysics CFD study on the part-to-part gap during remote laser welding of copper-to-steel battery tab connectors with beam wobbling," Procedia CIRP **111**, 484–489 (2022).

[4] M. Chelladurai Asirvatham, S. Collins, and I. Masters, "Laser wobble welding of steel to aluminium busbar joints for Li-ion battery packs," Opt. Laser Technol. **151**, 108000 (2022).

[5] M. J. Brand, P. A. Schmidt, M. F. Zaeh, and A. Jossen, "Welding techniques for battery cells and resulting electrical contact resistances," J. Energy Storage **1**, 7–14 (2015).

[6] I. Balz, E. Abi Raad, E. Rosenthal, R. Lohoff, A. Schiebahn, U. Reisgen, and M. Vorländer, "Process monitoring of ultrasonic metal welding of battery tabs using external sensor data," J. Adv. Join. Process. **1**, 100005 (2020).

[7] A. Gullino, P. Matteis, and F. D. Aiuto, "Review of aluminum-to-steel welding technologies for car-body applications," Metals **9**, 315 (2019).

[8] T. Sun, P. Franciosa, and D. Ceglarek, "Effect of focal position offset on joint integrity of AA1050 battery busbar assembly during remote laser welding," J. Mater. Res. Technol. **14**, 2715–2726 (2021).

[9] K. Martinsen, S. J. Hu, and B. E. Carlson, "Joining of dissimilar materials," CIRP Ann. Manuf. Technol. **64**, 679–699 (2015).

29 November 2023 14:30:58

[10]ASM International, *Soldering: Understanding the Basics* (ASM International, Novelty, OH, 2014).

[11]H. R. Kotadia, P. Franciosa, S. Jabar, and D. Ceglarek, "Remote laser welding of Zn coated IF steel and 1050 aluminium alloy: Processing, microstructure and mechanical properties," J. Mater. Res. Technol. **19**, 449–465 (2022).

[12]H. Springer, A. Kostka, E. J. Payton, D. Raabe, A. Kaysser-Pyzalla, and G. Eggeler, "On the formation and growth of intermetallic phases during interdiffusion between low-carbon steel and aluminum alloys," Acta Mater. **59**, 1586–1600 (2011).

[13]X. G. Wang, X. D. Yuan, J. N. Li, and X. G. Li, "Influence of interfacial intermetallic compounds on the electrical characterization of Cu/Al joints produced by flash welding and diffusion brazing," Mater. Res. **23**, e20200325 (2020).

[14]P. Schmalen and P. Plapper, "Resistance measurement of laser welded dissimilar Al/Cu joints," J. Laser Micro/Nanoeng. **12**, 189–194 (2017).

[15]A. Sadeghian and N. Iqbal, "A review on dissimilar laser welding of steel-copper, steel-aluminum, aluminum-copper, and steel-nickel for electric vehicle battery manufacturing," Opt. Laser Technol. **146**, 107595 (2022).

[16]O. Seffer, R. Pfeifer, A. Springer, and S. Kaierle, "Investigations on laser beam welding of different dissimilar joints of steel and aluminum alloys for automotive lightweight construction," Phys. Procedia **83**, 383–395 (2016).

[17]S. Jabar, A. B. Barenji, P. Franciosa, H. R. Kotadia, and D. Ceglarek, "Effects of the adjustable ring-mode laser on intermetallic formation and mechanical properties of steel to aluminium laser welded lap joints," Mater. Des. **227**, 111774 (2023).

[18]M. Mohammadpour, N. Yazdian, G. Yang, H. P. Wang, B. Carlson, and R. Kovacevic, "Effect of dual laser beam on dissimilar welding-brazing of aluminum to galvanized steel," Opt. Laser Technol. **98**, 214–228 (2018).

[19]M. Rasch, C. Roider, S. Kohl, J. Strauß, N. Maurer, K. Y. Nagulin, and M. Schmidt, "Shaped laser beam profiles for heat conduction welding of aluminium-copper alloys," Opt. Lasers Eng. **115**, 179–189 (2019).

[20]L. Wang, Masoud Mohammadpour, Xiangdong Gao, Jean-Philippe Lavoie, Klaus Kleine, Fanrong Kong, and Radovan Kovacevic, "Adjustable ring mode (ARM) laser welding of stainless steels," Opt. Lasers Eng. **137** (2021).

[21]H. Xia, W. Tao, L. Li, C. Tan, K. Zhang, and N. Ma, "Effect of laser beam models on laser welding–brazing Al to steel," Opt. Laser Technol. **122**, 105845 (2020).

[22]See https://www.matweb.com/index.aspx for "MatWeb material property data" (accessed June 21, 2023).

[23]Lumentum Operations LLC, see https://www.lumentum.com/en/commercial-lasers/products/kw-fiber-and-direct-diode-lasers for "kW fiber and direct-diode lasers" (2023) (accessed September 18, 2023).

[24]L. Cui, H. Chen, B. Chen, and D. He, "Welding of dissimilar steel/Al joints using dual-beam lasers with side-by-side configuration," Metals **8**, 1017–1038 (2018).

[25]M. J. L, "Fe-Al binary phase diagram," in *Alloy Phase Diagrams* (ASM International, Novelty, OH, 1992).

[26]J. Yang, J. P. Oliveira, Y. Li, C. Tan, C. Gao, Y. Zhao, and Z. Yu, "Laser techniques for dissimilar joining of aluminum alloys to steels: A critical review," J. Mater. Process. Technol. **301**, 117443 (2022).

[27]H. Bishara, S. Lee, T. Brink, M. Ghidelli, and G. Dehm, "Understanding grain boundary electrical resistivity in Cu: The effect of boundary structure," ACS Nano **15**, 16607–16615 (2021).

29 November 2023 14:30:58